

激光选区熔化 AlSi10Mg 合金退火后的显微组织和断裂韧性研究

唐鹏钧^{1,2,3}, 闫泰起², 李沛勇^{1,2,3}, 郭绍庆², 楚瑞坤⁴, 陈冰清^{2*}

¹中国航发北京航空材料研究院铝合金所, 北京 100095;

²中国航发北京航空材料研究院 3D 打印研究与工程技术中心, 北京 100095;

³北京市先进铝合金材料及应用工程技术研究中心, 北京 100095;

⁴飞而康快速制造科技有限责任公司, 江苏 无锡 214145

摘要 采用激光选区熔化技术制备了 AlSi10Mg 合金,研究了退火态合金的显微组织和不同开口方向紧凑拉伸试样的断裂韧性,分析了合金显微组织对断裂韧性的影响。结果表明:退火态合金中仍存在明显的组织各向异性,不同开口方向试样的断裂韧性出现差异;X-Y 与 Y-Z 开口方向试样的断裂韧性相当,其 J 积分值和裂纹尖端张开位移分别约为 430 kJ/m^2 和 0.8 mm ,而 Z-Y 开口方向试样的仅约为 250 kJ/m^2 和 0.47 mm 。由于熔池边界附近的组织相对粗大,小角度晶界比例较高,故 Z-Y 开口方向试样的裂纹倾向于沿熔池边界扩展,导致断裂韧性较低;而熔池内部组织相对细小,大角度晶界比例较高,因此 X-Y 与 Y-Z 开口方向试样在裂纹穿过熔池内部扩展时表现出的断裂韧性更好。

关键词 激光技术; 激光选区熔化; AlSi10Mg 合金; 显微组织; 断裂韧性; 各向异性

中图分类号 TG146.2

文献标志码 A

doi: 10.3788/CJL202148.1002001

1 引言

激光选区熔化(SLM)是以高能激光束为热源,实现金属粉末逐层重熔和凝固的一种金属材料增材制造技术^[1]。该技术能够实现复杂零部件的近净成型,且具有周期短、材料利用率高等特点,已被广泛应用于航空航天领域中铝合金、钛合金、高温合金和高强度钢等零部件的制备^[2-3]。近年来,国内外学者针对激光选区熔化 AlSi10Mg 合金的成形参数、组织和性能进行了研究,探索并优化了该合金的成形工艺,分析了沉积态与热处理态合金的组织和性能^[4-8]。相关研究结果显示^[9-13],激光选区熔化 AlSi10Mg 合金在沉积态下具有较高的残余应力和明显的组织各向异性。热处理可以有效降低或消除残余应力,弱化组织和性能的各向异性,但同时也易引起组织粗化,导致强度下降^[14]。目前,大多数研究重点关注热处理后激光选区熔化 AlSi10Mg 合金

的室温拉伸强度和疲劳性能,而对该合金断裂韧性的关注较少。Hitzler 等^[15]研究了激光选区熔化 AlSi10Mg 合金在沉积态下的断裂韧性,结果显示,沉积态合金的断裂韧性存在各向异性,表现为裂纹表面平行于成形方向时断裂韧性(K_{IC})最小,垂直于成形方向时 K_{IC} 最高;但他们未对断裂韧性各向异性的原因进行深入分析。Uzan 等^[16]基于裂纹深度估算了不同状态下激光选区熔化 AlSi10Mg 合金的应力强度因子(K_{cr}),结果发现,沉积态合金的 K_{cr} 值最高,去应力退火及其热等静压后的 K_{cr} 值均显著下降。所查资料显示,还未有文献对退火态合金断裂韧性的各向异性进行报道。为探索激光选区熔化 AlSi10Mg 合金退火处理后断裂韧性的各向异性,本文在前期开展不同退火温度下合金残余应力和室温拉伸性能研究的基础上,采用优选的退火温度($275 \text{ }^\circ\text{C}$)对沉积态合金进行退火处理,研究了退火态合金在不同开口方向下的断裂韧性,并分析

收稿日期: 2020-10-23; 修回日期: 2020-11-06; 录用日期: 2020-11-19

*E-mail: hwtkjebq1984@163.com

了退火态合金断裂韧性各向异性的原因。

2 试验材料及方法

试验所用 AlSi10Mg 合金粉末的名义成分为 Al-10Si-0.35Mg, 该粉末采用气雾化工艺制备而成。在 XLine 1000R 型 Concept Laser 设备上采用棋盘扫描策略成形, 成形过程中采用惰性气体进行保护, 成形环境中氧的体积分数不超过 0.1%, 激光束扫描方向逐层旋转 90°, 如图 1 所示。成形工艺参数如下: 层厚 40 μm, 激光功率 350~500 W, 扫描速率 1500~1800 mm/s, 扫描间距 0.13~0.18 mm。利用线切割将沉积态试块从基板上取下, 并于 275 °C 退火处理 2 h。

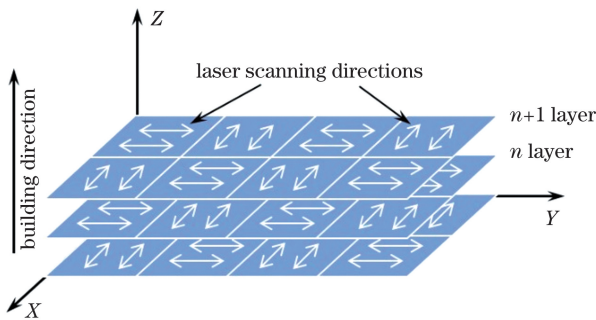


图 1 激光选区熔化成形扫描策略示意图

Fig. 1 Schematic of scanning strategy for selective laser melting

从退火态合金中切取尺寸为 7 mm × 7 mm × 5 mm 的试块, 依次采用 120[#]、240[#]、400[#]、800[#]、1200[#]、2000[#] 金刚石砂纸进行研磨; 再在 LectroPol-5 型电解抛光仪上进行抛光, 抛光液为高氯酸乙醇溶液(高氯酸与乙醇的体积比为 1:9), 起始电压为 35 V, 时间 20 s。利用 Leica DM4000 型光学显微镜观察退火态合金的显微组织; 采用 FEI nano 450 型场发射扫描电子显微镜(SEM)观察退火态合金的显微组织和紧凑拉伸试样的断口形貌, 工作电压为 10 kV; 利用振动抛光技术制备背散射电子衍射试样, 采用 Hikari XP 型背散射电子衍射仪在 JEOL-7900 型场发射扫描电子显微镜(SEM)上观察合金中的晶粒形貌、晶粒取向及晶界分布情况。

切取 X/Y 方向和 Z 方向的室温拉伸试样(如图 2 所示)各 4 个, 将其加工成直径为 5 mm 的圆形试样, 然后根据 GB/T 228.1—2010 在 AG-IS250kN 型万能材料试验机上进行室温拉伸性能测试。同一方向 4 个室温拉伸试样的测试结果取平均

值用于计算平面应变断裂韧度 K_{IC} 。按图 2 所示的开口方向加工紧凑拉伸试样, 每种开口方向各 2 个试样; 再根据 GB/T 4161—2007 的规定加工试样, 取试样宽度 W 为 70 mm; 最后在 MTS-250kN 型疲劳试验机上进行平面应变断裂韧度 K_{IC} 测试, 记录测试过程中的载荷和裂纹开口位移。

按照 GB/T 4161—2007《金属材料平面应变断裂韧度 K_{IC} 试验方法》的规定计算平面应变断裂韧度 K_{IC} 的条件值 K_Q [计算公式见(1)式], 并根据该标准规定的 K_{IC} 评判准则判定测试结果的有效性。 J 积分按(2)式进行计算^[17-19]。

$$K_Q = \frac{F_Q}{B \sqrt{W}} \times f(a/W), \quad (1)$$

$$J = \frac{2A_{tot}}{Bb}, \quad (2)$$

式中: F_Q 为载荷条件值, 可按 GB/T 4161—2007 规定的方法从载荷-裂纹开口位移曲线中获得; W 为试样宽度; $f(a/W)$ 为与 a/W 相关的函数, 可按 GB/T 4161—2007 中的式(C.1)计算得到; A_{tot} 为载荷-裂纹开口位移曲线下方的总面积; B 为试样厚度; b 为韧带尺寸, $b = W - a$; a 为预制裂纹长度。

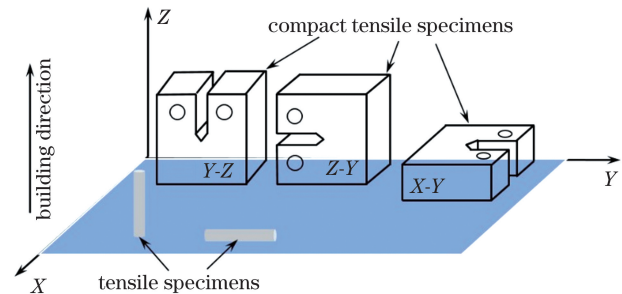


图 2 拉伸试样和紧凑拉伸试样的取样示意图

Fig. 2 Sketch map of tensile samples and compact tensile specimens

裂纹尖端张开位移(CTOD, δ)的计算公式为^[17]

$$\delta = \frac{J}{m\sigma_Y}, \quad (3)$$

式中: σ_Y 指有效屈服应力, 为规定非比例延伸强度 ($R_{p0.2}$) 和抗拉强度 (R_m) 的平均值; m 为约束系数。约束系数 m 的计算公式为^[17]

$$m = A_0 - A_1 \left(\frac{R_{p0.2}}{R_m} \right) + A_2 \left(\frac{R_{p0.2}}{R_m} \right)^2 - A_3 \left(\frac{R_{p0.2}}{R_m} \right)^3. \quad (4)$$

对于紧凑拉伸试样, $A_0 = 3.62$, $A_1 = 4.21$, $A_2 = 4.33$, $A_3 = 2.00$ ^[17]。断裂韧度的计算参数见表 1。

表 1 不同开口方向紧凑拉伸试样断裂韧度的计算参数

Table 1 Calculation parameters of fracture toughness for compact tensile specimens with different opening directions

No.	Direction	W /mm	B /mm	a /mm	b /mm	R_m /MPa	$R_{p0.2}$ /MPa	σ_V /MPa	$R_{p0.2} / R_m$	m
X-Y-1	X-Y	69.97	34.68	35.51	34.46	301.0	187.0	244.0	0.62	2.20
X-Y-2		69.98	35.20	35.38	34.60					
Y-Z-1	Y-Z	70.01	35.10	35.84	34.17	301.0	187.0	244.0	0.62	2.20
Y-Z-2		69.98	34.97	35.53	34.45					
Z-Y-1	Z-Y	69.99	35.00	35.55	34.44	300.5	188.3	244.4	0.63	2.20
Z-Y-2		70.01	35.01	35.77	34.24					

3 分析与讨论

3.1 显微组织

图 3 为退火态合金的显微组织。可以发现:在退火态合金中,平行于成形方向的组织呈现出“鱼鳞状”熔池逐层堆叠的形貌,而垂直于成形方向的

组织则呈现为熔池相互交织的结构。这说明,在该温度下退火后,沉积态合金中典型的“鱼鳞状”熔池及其逐层堆叠和相互交织的结构未发生显著变化,形态学织构得以保留。研究显示^[14],当热处理温度为 540 °C (固溶温度) 时,熔池形貌会完全消失。

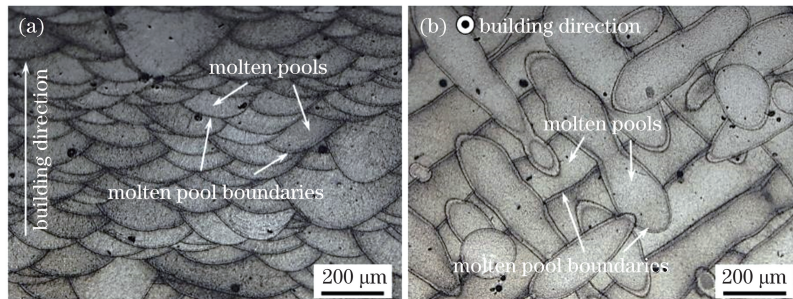


图 3 退火态合金的显微组织。(a) 平行于成形方向;(b) 垂直于成形方向

Fig. 3 Microstructures of annealed alloy. (a) Parallel to building direction; (b) perpendicular to building direction

进一步对退火态合金的显微组织进行观察可以发现,该状态下的合金主要由铝基体和网状分布的共晶硅颗粒组成,如图 4 所示。根据共晶硅颗粒及其分布的网格尺寸的大小,可大致识别出熔池和熔池边界区域。熔池边界上的共晶硅颗粒尺寸较大,网格尺寸也较大,而熔池内部的共晶硅颗粒及其网格尺寸均较小。此外,在平行和垂直于成形方向上的组织中,共晶硅的网格形貌显著不同:在平行于成形方向上,共晶硅分布的网格形状为长条形,如

图 4(a) 所示;而在垂直于成形方向上,共晶硅分布的网格形状更倾向于等轴状,如图 4(b) 所示。由于凝固过程中熔池边界附近组织的冷却速率较低,故形成的网状共晶硅组织较为粗大;而熔池内部的熔体在高冷速下形成了相对细小的网状共晶硅组织^[20-21]。在退火过程中,硅原子发生扩散和聚集,使得共晶硅发生了一定程度的钝化和粗化^[4, 22]。但由于退火温度较低,退火时间较短,不足以使网状共晶硅形貌发生显著改变。

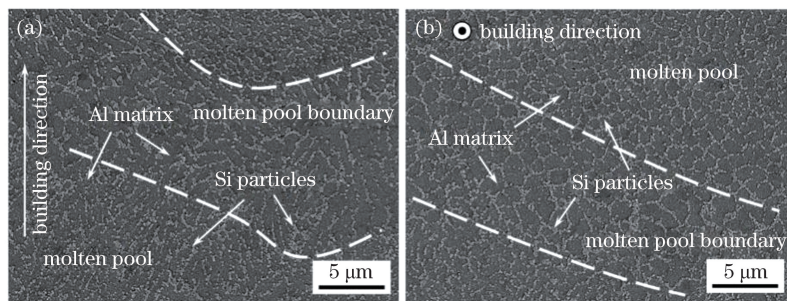


图 4 退火态合金的 SEM 形貌。(a) 平行于成形方向;(b) 垂直于成形方向

Fig. 4 SEM morphologies of annealed alloy. (a) Parallel to building direction; (b) perpendicular to building direction

图 5 为退火态合金的晶粒形貌及晶界分布。结果显示:在平行于成形方向上,退火态合金的晶粒主要为柱状晶,晶粒的生长方向垂直于熔池边界并指向熔池中心;在垂直于成形方向上,晶粒为等轴晶。此外,对比晶粒尺寸可以发现,熔池边界附近的晶粒通常更为细小,而熔池内部的晶粒较为粗大。从晶粒取向来看,在平行于成形方向的组织中,晶粒取向相对随机,未见明显的择优取向,如图 5(a)所示;但在垂直于成形方向上,晶粒则表现出较为明显的择优取向,主要体现在熔池边界附近的晶粒倾向于 $\langle 101 \rangle$ 或 $\langle 111 \rangle$ 方向生长,而熔池内部晶粒的取向多为 $\langle 001 \rangle$ 方向,如图 5(b)所示。分析认为,晶粒出现这种择优取向与凝固过程中熔融合金的晶体生长形态有关:当

立方晶体材料以柱状晶生长时,易沿 $\langle 001 \rangle$ 晶向生长^[23]。

从晶界分布来看,退火态合金中存在大角度晶界和小角度晶界,如图 5(c)和图 5(d)所示。统计结果显示,图 5(c)中小角度晶界约占 34.1%,大角度晶界约占 65.9%。观察还可以发现,大角度晶界在整个组织中大量存在,而小角度晶界则主要分布于熔池内部中心区域和熔池边界附近。因此,在熔池中心区域或熔池边界附近的局部组织中,小角度晶界的占比更高。由于小角度晶界对毗邻晶粒之间位错滑移的阻碍作用较小,因此裂纹更容易通过小角度晶界扩展。相比之下,大角度晶界两侧晶粒之间的取向差较大,位错易被堵塞在晶界附近,从而有助于阻碍裂纹的扩展。

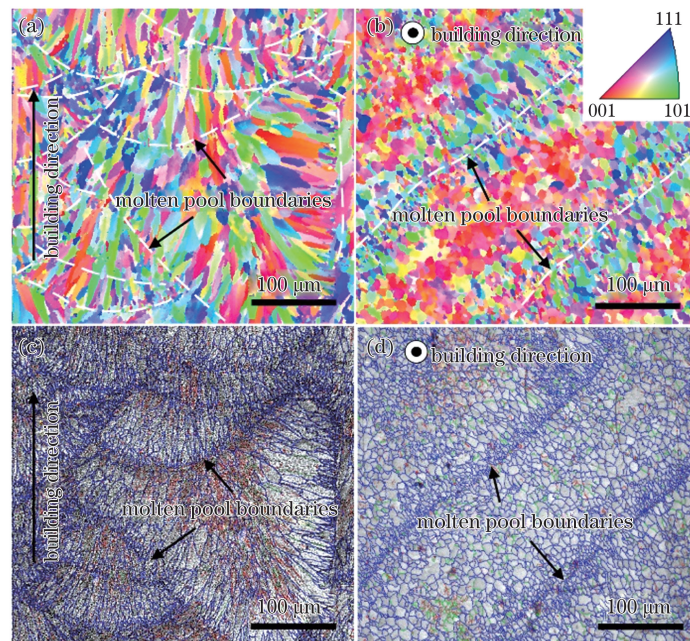


图 5 退火态合金的晶粒形貌及晶界分布。(a)平行于成形方向的晶粒形貌;(b)垂直于成形方向的晶粒形貌;(c)平行于成形方向的晶界分布;(d)垂直于成形方向的晶界分布

Fig. 5 Grain morphology and grain boundary distribution of annealed alloy. (a) Grain morphology parallel to building direction; (b) grain morphology perpendicular to building direction; (c) grain boundary distribution parallel to building direction; (d) grain boundary distribution perpendicular to building direction

3.2 断裂韧性

图 6 为不同开口方向紧凑拉伸试样的载荷-裂纹开口位移曲线。可以看出:在载荷上升初期,载荷与裂纹开口位移之间存在一定的线性关系,这种线性关系主要由材料的弹性变形引起;随着载荷的进一步增加,材料发生塑性变形,并且亚临界裂纹开始生长,载荷与裂纹开口位移之间变为非线性关系;当载荷达到临界值时,裂纹失稳迅速扩展,最终导致材料断裂。对比图 6 可以发现,不同开口方向紧凑拉伸试样的最大载荷存在差异,其中 X-Y、Y-Z、Z-Y

试样最大载荷的平均值分别约为 47.9, 47.0, 42.7 kN。这说明, X 方向和 Y 方向组织承受裂纹扩展的最大载荷基本相当,均略高于 Z 方向的组织。

表 2 为不同开口方向紧凑拉伸试样断裂韧性的试验结果。结果显示:开口方向为 X-Y 的试样的 K_Q 计算值最高,开口方向为 Z-Y 的试样最低;不同开口方向紧凑拉伸试样的 $2.5(K_Q/R_{p0.2})^2$ 的计算结果均超过了 99 mm,故试样厚度(B)、预制裂纹长度(a)和韧带尺寸(b)均不满足 GB/T 4161—2007 规定的 K_{IC} 评判准则要求;同时,最大载荷与载荷

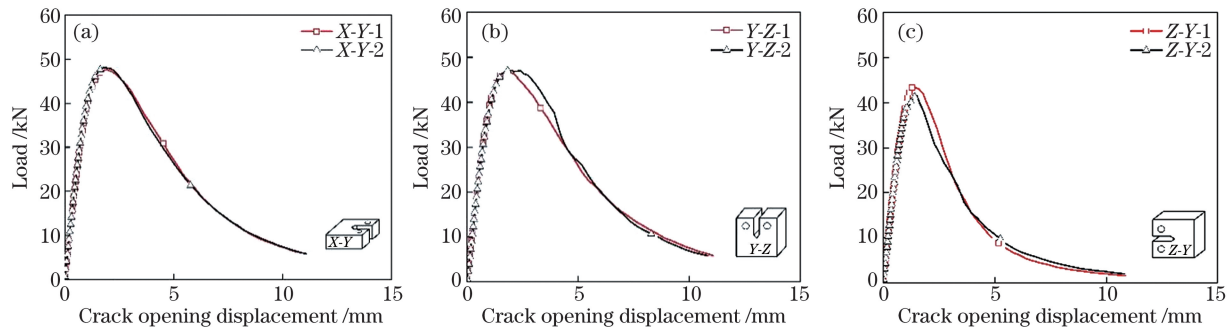


图 6 不同开口方向紧凑拉伸试样的载荷-裂纹开口位移曲线。(a) X-Y; (b) Y-Z; (c) Z-Y

Fig. 6 Load versus crack opening displacement curves of compact tensile specimens with different opening directions.

(a) X-Y; (b) Y-Z; (c) Z-Y

条件值的比值(F_{\max}/F_Q)均超过了 1.1。因此,获得的 K_Q 无效,也无法通过本试验获得有效的 K_{IC} 。

从表 2 中不同开口方向试样的 J 积分值可以看出,X-Y 和 Y-Z 开口方向试样的 J 积分值均达到了 430 kJ/m^2 左右,而开口方向为 Z-Y 的试样仅约为 250 kJ/m^2 。由此说明,当裂纹表面平行于成形方向时,裂纹扩展所需的能量基本相当,而裂纹表面垂直于成形方向时,裂纹扩展所需要的能量明显降低。由(2)式可知, J 积分值与载荷-裂纹开口位移曲线下方的总面积成正比,故图 6 中载荷-裂纹开口位移曲线下方的总面积也可以直观地反映不同开口

方向试样中裂纹扩展所需能量的差异。

此外,表 2 中还给出了不同开口方向试样的 CTOD 计算结果。对比后发现:开口方向为 X-Y 和 Y-Z 的试样的 CTOD 值相同,均约为 0.8 mm ,而开口方向为 Z-Y 试样的 CTOD 值仅为 0.47 mm 。材料萌生裂纹后,在载荷作用下,裂纹尖端附近的塑性区导致裂纹尖端表面张开。当裂纹表面平行于成形方向时,裂纹尖端表面张开位移达到 0.8 mm 后,裂纹发生失稳扩展;当裂纹表面垂直于成形方向时,裂纹发生失稳扩展对应的 CTOD 临界值仅为 0.47 mm 。

表 2 不同开口方向紧凑拉伸试样的试验结果

Table 2 Test results of compact tensile specimens with different opening directions

No.	Direction	F_Q/kN	$K_Q/(\text{MPa}\sqrt{\text{m}})$	$2.5(K_Q/R_{p0.2})^2/\text{mm}$	F_{\max}/kN	F_{\max}/F_Q	$J/(\text{kJ}\cdot\text{m}^{-2})$	CTOD/mm
X-Y-1	X-Y	38.74	41.81	124.97	47.703	1.23	436.06	0.81
X-Y-2		39.03	41.24	121.59	48.119	1.23	430.00	0.80
Y-Z-1	Y-Z	38.26	41.32	122.06	46.819	1.22	429.64	0.80
Y-Z-2		38.08	40.75	118.72	47.098	1.24	431.60	0.81
Z-Y-1	Z-Y	36.35	41.00	118.52	43.673	1.20	252.15	0.47
Z-Y-2		34.72	37.48	99.05	41.579	1.20	251.30	0.47

综上所述,X-Y 和 Y-Z 开口方向试样的断裂韧性相当,且均高于 Z-Y 开口方向试样。结合显微组织分析认为:X-Y 和 Y-Z 开口方向试样的裂纹表面均平行于成形方向,对应的组织为熔池逐层堆叠形貌;而 Z-Y 开口方向试样的裂纹表面垂直于成形方向,对应的组织为熔池相互交织的形貌。由此说明,不同开口方向试样断裂韧性的差异与组织各向异性有关。

3.3 断口形貌

图 7 为不同开口方向紧凑拉伸试样过载区的断口形貌。结果显示,X-Y、Y-Z 和 Z-Y 开口方向试样

断口的过载区均存在大量韧窝,表现为韧性断裂。根据韧窝尺寸可以大致区分断口中熔池内部和熔池边界组织,如图中虚线所示。从图 7(a)~(c)可以看出,X-Y 和 Y-Z 开口方向试样断口上的韧窝呈长条形,而 Z-Y 开口方向试样断口上的韧窝多呈等轴状。这主要是由不同方向组织形貌差异导致的。对比韧窝底部的共晶硅颗粒可以发现,X-Y 和 Y-Z 开口方向试样断口上共晶硅颗粒的尺寸比 Z-Y 开口方向试样上的小。结合图 4 中熔池边界和熔池内部共晶硅颗粒的尺寸差异可知,Z-Y 开口方向紧凑拉伸试样的裂纹扩展面接近熔池边界。由于在激光选

区熔化 AlSi10Mg 合金中,硅颗粒发挥着阻碍位错迁移的作用。当位错堆积引起的应力足够大时,位错将切过硅颗粒形成层错或孪晶^[24];但尺寸相对粗大的硅颗粒会导致合金的强度和塑性下降^[25]。因此,当熔池边界附近存在相对粗大的共晶硅颗粒和较高比例的小角度晶界时,组织对裂纹扩展的阻碍

作用较小,导致 Z-Y 开口方向试样的 J 积分和 CTOD 值较低。相比之下,X-Y 和 Y-Z 开口方向试样的裂纹扩展面穿过熔池内部,而熔池内部的共晶硅颗粒细小,大角度晶界比例较高,可以更好地发挥阻碍位错迁移和裂纹扩展的作用;故 X-Y、Y-Z 开口方向紧凑拉伸试样的 J 积分和 CTOD 值较高。

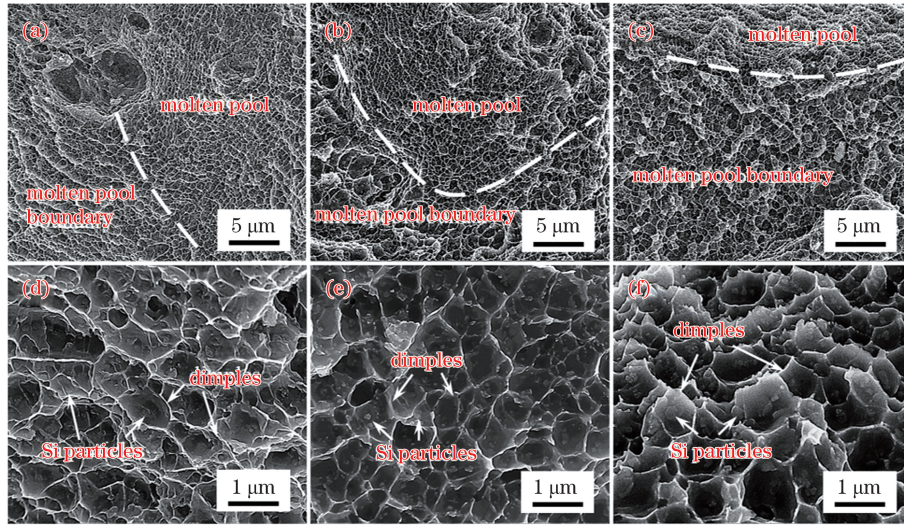


图 7 不同开口方向紧凑拉伸试样过载区的断口形貌。(a)(d) X-Y;(b)(e) Y-Z;(c)(f) Z-Y

Fig. 7 Fracture graphs of over-load zone for compact tension specimens with different opening directions. (a)(d) X-Y; (b)(e) Y-Z; (c)(f) Z-Y

4 结 论

通过研究退火态激光选区熔化 AlSi10Mg 合金的显微组织和不同开口方向试样的断裂韧性,得到了以下主要结论:

1) 退火后合金的组织 and 断裂韧性均存在各向异性。当裂纹表面平行于成形方向时,试样的断裂韧性较高;当裂纹表面垂直于成形方向时,断裂韧性较低。

2) 组织各向异性以及熔池边界与熔池内部的组织差异是导致断裂韧性出现各向异性的主要原因。

3) 激光选区熔化 AlSi10Mg 合金的断裂韧性较好,按照通用测试方法(GB/T 4161—2007)难以获得有效的 K_{IC} 值,可能需要采用专门的铝合金线弹性平面应变断裂韧性试验方法(如 ASTM B645)进行研究。

参 考 文 献

- [1] Gu D D, Zhang H M, Chen H Y, et al. Laser additive manufacturing of high-performance metallic aerospace components[J]. Chinese Journal of Lasers, 2020, 47(5): 0500002.
顾冬冬, 张红梅, 陈洪宇, 等. 航空航天高性能金属材料构件激光增材制造[J]. 中国激光, 2020, 47(5): 0500002.
- [2] Yang Y Q, Wu S B, Zhang Y, et al. Application progress and prospect of fiber laser in metal additive manufacturing[J]. Chinese Journal of Lasers, 2020, 47(5): 0500012.
杨永强, 吴世彪, 张越, 等. 光纤激光器在金属增材制造中的应用进展及展望[J]. 中国激光, 2020, 47(5): 0500012.
- [3] Yao Y S, Wang J, Chen Q B, et al. Research status of defects and defect treatment technology for laser additive manufactured products[J]. Laser & Optoelectronics Progress, 2019, 56(10): 100004.
姚燕生, 汪俊, 陈庆波, 等. 激光增材制造产品缺陷及其处理技术研究现状[J]. 激光与光电子学进展, 2019, 56(10): 100004.
- [4] Zhang W Q, Zhu H H, Hu Z H, et al. Study on the selective laser melting of AlSi10Mg[J]. Acta Metallurgica Sinica, 2017, 53(8): 918-926.
张文奇, 朱海红, 胡志恒, 等. AlSi10Mg 的激光选区熔化成形研究[J]. 金属学报, 2017, 53(8): 918-926.
- [5] Yan T Q, Tang P J, Chen B Q, et al. Effect of annealing temperature on microstructure and tensile properties of AlSi10Mg alloy fabricated by selective laser melting[J]. Journal of Mechanical Engineering, 2020, 56(8): 37-45.

- 闫泰起, 唐鹏钧, 陈冰清, 等. 退火温度对激光选区熔化 AlSi10Mg 合金微观组织及拉伸性能的影响[J]. 机械工程学报, 2020, 56(8): 37-45.
- [6] Ngnekou J N D, Nadot Y, Henaff G, et al. Fatigue properties of AlSi10Mg produced by additive layer manufacturing[J]. *International Journal of Fatigue*, 2019, 119: 160-172.
- [7] Zhou L, Mehta A, Schulz E, et al. Microstructure, precipitates and hardness of selectively laser melted AlSi10Mg alloy before and after heat treatment[J]. *Materials Characterization*, 2018, 143: 5-17.
- [8] Rosenthal I, Shneck R, Stern A, et al. Heat treatment effect on the mechanical properties and fracture mechanism in AlSi10Mg fabricated by additive manufacturing selective laser melting process[J]. *Materials Science and Engineering A*, 2018, 729: 310-322.
- [9] Hou W, Chen J, Chu S L, et al. Anisotropy of microstructure and tensile properties of AlSi10Mg formed by selective laser melting[J]. *Chinese Journal of Lasers*, 2018, 45(7): 0702003.
- 侯伟, 陈静, 储松林, 等. 选区激光熔化成形 AlSi10Mg 组织与拉伸性能的各向异性研究[J]. *中国激光*, 2018, 45(7): 0702003.
- [10] Jiang X H, Ye T, Zhu Y H, et al. Effect of process parameters on residual stress in selective laser melting of AlSi10Mg [J]. *Materials Science and Technology*, 2020, 36(3): 342-352.
- [11] Padovano E, Badini C, Pantarelli A, et al. A comparative study of the effects of thermal treatments on AlSi10Mg produced by laser powder bed fusion [J]. *Journal of Alloys and Compounds*, 2020, 831: 154822.
- [12] Strumza E, Yeheskel O, Hayun S, et al. The effect of texture on the anisotropy of thermophysical properties of additively manufactured AlSi10Mg[J]. *Additive Manufacturing*, 2019, 29: 100762.
- [13] Zhang Y J, Yu M H, Yang R X, et al. Effects of rare earth Sc on properties of laser-melted AlSi10Mg alloy[J]. *Chinese Journal of Lasers*, 2020, 47(8): 0802006.
- 张宇杰, 于梅花, 杨瑞霞, 等. 稀土 Sc 对激光制备 AlSi10Mg 合金性能的影响[J]. *中国激光*, 2020, 47(8): 0802006.
- [14] Yu K B, Liu Y Z, Yang C Y, et al. Effects of heat treatment on microstructures and mechanical properties of AlSi10Mg alloy produced by selective laser melting[J]. *Materials Science and Engineering of Powder Metallurgy*, 2018, 23(3): 298-305.
- 余开斌, 刘允中, 杨长毅, 等. 热处理对选区激光熔化成形 AlSi10Mg 合金显微组织及力学性能的影响[J]. *粉末冶金材料科学与工程*, 2018, 23(3): 298-305.
- [15] Hitzler L, Hirsch J, Schanz J, et al. Fracture toughness of selective laser melted AlSi10Mg [J]. *Proceedings of the Institution of Mechanical Engineers: Journal of Materials Design and Applications*, 2019, 233(4): 615-621.
- [16] Uzan N E, Shneck R, Yeheskel O, et al. Fatigue of AlSi10Mg specimens fabricated by additive manufacturing selective laser melting (AM-SLM) [J]. *Materials Science and Engineering A*, 2017, 704: 229-237.
- [17] Zhu X K, Joyce J A. Review of fracture toughness (G, K, J, CTOD, CTOA) testing and standardization[J]. *Engineering Fracture Mechanics*, 2012, 85: 1-46.
- [18] Meyers M A, Chawla K K. *Mechanical behavior of materials*[M]. 2nd ed. Cambridge: Cambridge University Press, 2008: 765-814.
- [19] Kumar N, Owolabi G M, Jayaganthan R, et al. Correlation of fracture toughness with microstructural features for ultrafine-grained 6082 Al alloy [J]. *Fatigue & Fracture of Engineering Materials & Structures*, 2018, 41(9): 1884-1899.
- [20] Li X P, Wang X J, Saunders M, et al. A selective laser melting and solution heat treatment refined Al-12Si alloy with a controllable ultrafine eutectic microstructure and 25% tensile ductility [J]. *Acta Materialia*, 2015, 95: 74-82.
- [21] Rao H, Giet S, Yang K, et al. The influence of processing parameters on aluminium alloy A357 manufactured by selective laser melting[J]. *Materials & Design*, 2016, 109: 334-346.
- [22] Zhang C C, Zhu H H, Liao H L, et al. Effect of heat treatments on fatigue property of selective laser melting AlSi10Mg [J]. *International Journal of Fatigue*, 2018, 116: 513-522.
- [23] Thijs L, Kempen K, Kruth J P, et al. Fine-structured aluminium products with controllable texture by selective laser melting of pre-alloyed AlSi10Mg powder [J]. *Acta Materialia*, 2013, 61(5): 1809-1819.
- [24] Kim D K, Hwang J H, Kim E Y, et al. Evaluation of the stress-strain relationship of constituent phases in AlSi10Mg alloy produced by selective laser melting using crystal plasticity FEM [J]. *Journal of Alloys and Compounds*, 2017, 714: 687-697.
- [25] Tang M, Pistorius P C. Anisotropic mechanical behavior of AlSi10Mg parts produced by selective laser melting[J]. *JOM*, 2017, 69(3): 516-522.

Microstructures and Fracture Toughness of Annealed AlSi10Mg Alloy Formed by Selective Laser Melting

Tang Pengjun^{1,2,3}, Yan Taiqi², Li Peiyong^{1,2,3}, Guo Shaoqing², Chu Ruikun⁴,
Chen Bingqing^{2*}

¹Institute of Aluminum Alloy, AECC Beijing Institute of Aeronautical Materials, Beijing 100095, China;

²3D Printing Research and Engineering Technology Center, AECC Beijing Institute of Aeronautical Materials, Beijing 100095, China;

³Beijing Engineering Research Center of Advanced Aluminum Alloys and Applications, Beijing 100095, China;

⁴Falcon Fast Manufacturing Technology Co., Ltd., Wuxi, Jiangsu 214145, China

Abstract

Objective AlSi10Mg alloy, prepared by selective laser melting, is one of the most widely investigated aluminum alloys recently. At present, most studies focus on the tensile strengths and fatigue properties of as-built or heat-treated alloys. However, fracture toughness is reported rarely. A study on as-built alloys indicated that fracture toughness was anisotropic. The plane-strain fracture toughness (K_{IC}) is the lowest when the crack surface is parallel to the building direction, whereas it is the highest when the crack surface is perpendicular to the building direction. Heat treatment is beneficial to reduce or even eliminate the microstructural and property anisotropy and the residual stress. However, the anisotropy of fracture toughness and intrinsic principle for AlSi10Mg alloy after annealing have not been reported. Therefore, to explore the anisotropy of fracture toughness of annealed AlSi10Mg alloy prepared by selective laser melting, the alloy annealed at an optimum temperature is used to measure fracture toughness for different opening directions and analyze the reasons for fracture toughness anisotropy.

Methods AlSi10Mg alloy is fabricated on XLine 1000R Concept Laser equipment using atomized alloying powders. The selective laser melting process is performed by a checkerboard pattern scanning strategy under an argon atmosphere with the volume fraction of oxygen controlled below 0.1%. Then, as-built blocks are annealed at 275 °C for 2 h. The sample blocks, ground on a series of diamond sandpaper, are polished on the LectroPol-5 electrolytic machine. The microstructures, fracture morphologies, and grain boundary distribution are observed via optical microscopy, field emission scanning electron microscopy, and electron backscattered diffraction, respectively. The room temperature tensile properties in the X, Y and Z directions, analyzed via tensile tests according to GB/T 228.1—2010, are used to calculate K_{IC} . The compact tensile specimens with a width (W) of 70 mm in different opening directions are prepared and tested according to GB/T 4161—2007. The load and crack opening displacement during tests are recorded. The conditional values of K_{IC} (K_Q) for different compact tensile specimens are calculated, and their validity are evaluated according to GB/T 4161—2007. Finally, the J -integral value and crack tip opening displacements are computed for different opening direction samples.

Results and Discussions Both K_Q and K_{IC} are invalid for all compact tensile specimens because the specimen thicknesses (B), pre-crack lengths (a), ligament lengths (b), and values of F_{max}/F_Q do not meet the requirements of K_Q and K_{IC} evaluation criteria stipulated by GB/T 4161—2007. Therefore, the fracture toughness and its anisotropy of annealed alloy are estimated by J -integral values and crack tip opening displacements. Results show that the J -integral value of the X-Y opening direction sample is approximately 430 kJ/m² (Table 2), which is the same as the Y-Z opening direction sample. Meanwhile, it is 250 kJ/m² for the Z-Y opening direction sample. Similarly, the crack tip opening displacements of the X-Y and Y-Z opening direction samples are also almost equal, approximately 0.8 mm. However, it is significantly lower for the Z-Y opening direction specimen, with a value of 0.47 mm, indicating that the fracture toughness of the annealed AlSi10Mg alloy is also anisotropic and similar to the as-built alloy. The results of microstructural observation indicate that the annealed alloy still exhibits the characteristics of “fish-scale” melt pools stacking layer by layer in parallel to the building direction, whereas it presents an interwoven morphology of melt pools as the structure is perpendicular to the building direction, indicating that the difference in fracture toughness in different directions is related to microstructural anisotropy. Because the structures near molten pool boundaries are relatively coarse and the ratio of low angle grain boundary is high, the

cracks of specimens in the Z - Y opening direction tend to propagate along molten pool boundaries, resulting in lower fracture toughness. However, the internal structures of the molten pool, existing with a higher ratio of high angle grain boundary, are relatively fine, inducing good fracture toughness when cracks propagate through the interior of molten pools for the X - Y and Y - Z opening direction samples.

Conclusions The microstructures and fracture toughness of annealed AlSi10Mg alloy are anisotropic. When a crack surface is parallel to the building direction, the fracture toughness is high, J -integral value and crack tip opening displacement are 430 kJ/m² and 0.8 mm, respectively. Meanwhile, it is lower when the crack surface is perpendicular to the building direction, and the J -integral value and crack tip opening displacement are just 250 kJ/m² and 0.47 mm, respectively. The microstructural anisotropy and diversity between molten pool boundaries and the internal structure of the molten pools are the reasons for fracture toughness anisotropy. Because the fracture toughness of the annealed AlSi10Mg alloy manufactured by selective laser melting is relatively high, it is difficult to obtain effective K_{IC} value according to the general test method, such as GB/T 4161—2007. It may be necessary to use a special linear elastic plane-strain fracture toughness test method, for instance, ASTM B645.

Key words laser technique; selective laser melting; AlSi10Mg alloy; microstructures; fracture toughness; anisotropy

OCIS codes 140.3390; 160.3900; 350.3850